

# What Gamma-Ray Deexcitation Lines Reveal about Solar Flares

R. J. Murphy and G. H. Share

*E. O. Hulburt Center for Space Research, Naval Research Laboratory, 4555 Overlook Ave., Washington, DC 20375, USA*

[ronald.murphy@nrl.navy.mil](mailto:ronald.murphy@nrl.navy.mil), [gerald.share@nrl.navy.mil](mailto:gerald.share@nrl.navy.mil)

## Abstract

Gamma-ray emission from solar flares reveals information about the nature of the accelerated particles and about the physical conditions of the medium through which the accelerated particles are transported. In this paper, we present the gamma-ray line production and loop transport models used in our calculations of high-energy emission. We discuss the calculated interaction time history, the depth distribution, the interacting-particle angular distribution, and fluence ratios of the narrow gamma-ray lines. We show the relationship between the  $\gamma$ -ray observables and the parameters of the transport and line-production models. For illustration, we use calculations of 4.44 MeV  $^{12}\text{C}$  nuclear deexcitation line production. Applications of the calculations to flare observations by both *SMM* and *RHESSI* are also presented.

Keywords: solar flares; gamma rays; abundances; particle acceleration

## 1. Introduction

Although it is generally accepted that the energy source for particle acceleration in solar flares is related to reconnection of coronal magnetic fields (Sturrock et al. 2001), the identification of the acceleration process(es) and an understanding of the physical conditions at the flare site are still open issues. Potential acceleration mechanisms include stochastic (via waves), shock (both drift and diffusive), and electric field acceleration (see, e.g., Miller et al. 1997 and Aschwanden 2002). Some of the ions accelerated in solar flares can escape from the Sun into interplanetary space. Information about these ions can be obtained from direct measurement of impulsive solar energetic particle events (Reames 2002). Other ions accelerated in flares remain trapped at the Sun and information about these ions can be obtained by observing the high-energy emissions that result from their nuclear interactions with the solar atmosphere. These interactions produce excited and radioactive nuclei, neutrons and pi-mesons. All of these products subsequently produce observable  $\gamma$ -rays via secondary processes and the neutrons that escape may be both directly observed in space and via their decay protons.

An overview of the flare phenomenon is shown in Figure 1. That this view is generally correct is supported by the image obtained with the Yohkoh satellite (and confirmed more recently by *RHESSI* observations) shown in the upper left of the Figure (Masuda et al. 1994). The gray-scale image shows soft X-ray emission, revealing the magnetic loop filled with hot plasma. The contours show hard X-ray sources, revealing both the footpoints of the loops where accelerated electrons interact and a source above the loop, possibly associated with the primary acceleration (see Aschwanden et al. 1996).

The measurable quantities associated with high-energy solar-flare emissions (e.g.,  $\gamma$ -ray line intensities, shapes, and time histories and escaping neutron spectra and time histories) convey information about the accelerated ions responsible for their production and about the physical conditions where the ions propagate and where they interact. *Acceleration parameters*, such as the number and spectral shape of the accelerated protons and  $\alpha$  particles (and thus their energy content), the acceleration/transport time history, and the relative abundances of the accelerated ions can be obtained from measured deexcitation line fluxes and flux ratios. This aspect of high-energy flare emission has been well-explored in past research (e.g., Ramaty et al. 1995).

However, the measurable quantities can also depend strongly on the physical conditions of the flare magnetic loop in which the particles transport from the acceleration site to the interaction region. These physical conditions are described by *physical parameters*, such as loop length, the level of pitch-angle scattering (PAS) within the loop, the degree of convergence of the loop magnetic field at the footpoints, and the density and temperature height-profile and elemental composition of the ambient flaring solar atmosphere where the

interactions take place. Analyses of high-energy solar-flare emissions therefore offer the potential to learn much more about the flare process than just particle acceleration.

In this paper we will concentrate on what can be learned about particle acceleration and the physical conditions of the flare loop using observations of  $\gamma$ -ray deexcitation lines. In §2 we discuss the transport and interaction model used and the associated acceleration and physical parameters. In §3 we discuss how the observable quantities associated with deexcitation  $\gamma$ -ray lines depend on these parameters.

## 2. Transport and interaction model

### 2.1 Transport model

Extracting information on the acceleration process and the conditions within the flare loop from  $\gamma$ -ray and neutron observations requires a transport and interaction model. A transport model was developed by Hua et al. (1989) in which a Monte Carlo simulation follows individual energetic ions through a flare loop until they either undergo a nuclear reaction or their energy falls below nuclear reaction thresholds. The most important aspects of ion transport are included in the model: energy losses due to Coulomb collisions, removal by nuclear reactions, magnetic mirroring in the convergent flux tube, and MHD pitch angle scattering.

The model consists of a semicircular coronal portion of length  $L$  and two straight portions extending vertically from the transition region through the chromosphere into the photosphere. Below the transition region, the magnetic field strength is assumed proportional to a power  $\delta$  of the pressure (Zweibel et al. 1983). Pitch angle scattering is characterized by  $\Lambda$ , the mean free path required for an arbitrary initial angular distribution to relax to an isotropic distribution (see the discussion in Hua et al. (1989) for a detailed discussion).  $\Lambda$  is assumed to be independent of particle energy. The level of PAS is then characterized by  $\lambda$ , the ratio of  $\Lambda$  to the loop half-length  $L_c (= L/2)$ . A particular height-density profile for the solar atmosphere (e.g., that of Avrett 1981) is assumed. The accelerated ions are released isotropically at the top of the loop with an assumed spectral shape, normalized so that there is one proton greater than 10 MeV. All species are assumed to share this same spectral shape. The ions are followed until they interact according to the cross section for the reaction being considered (typically near the loop footpoints in the chromosphere or upper photosphere) or thermalize. We assume a power law for the accelerated-particle spectral shape. Ramaty et al. (1995) showed that power laws are consistent with both the 1.634 MeV  $^{20}\text{Ne}$  / 6.129 MeV  $^{16}\text{O}$  and the 2.223 MeV neutron-capture / 4.439 MeV  $^{12}\text{C}$  measured line-fluence ratios. These ratios cover the particle energy range from  $\sim 2$  to  $\sim 30$  MeV nucleon $^{-1}$ . Ramaty et al. (1995) also found that power laws provided more acceptable derived Ne/O abundance ratios than did the Bessel functions used previously.

When an interaction occurs, the time after the initial release of the energetic ion, the location along the loop, and the direction of motion of the ion are recorded. The resulting interacting-particle angular distribution can then be used with the  $\gamma$ -ray line production code (discussed below) to calculate line shapes and shifts for a given observation direction. The attenuation of the  $\gamma$  ray along the line of sight can be calculated from the location of the interaction along the loop. The  $\gamma$ -ray emission is assumed isotropic in the excited-nucleus rest frame.

### 2.2 Gamma-ray production

A comprehensive treatment of nuclear deexcitation  $\gamma$ -ray line emission was given by Ramaty, Kozlovsky and Lingenfelter (1979). The resulting  $\gamma$ -ray line production code has been continuously updated (most recently by Kozlovsky et al. 2002) to incorporate new cross-section data and includes more than 100 explicit lines. This code calculates a complete  $\gamma$ -ray line spectrum along any observing direction from the flare site for any assumed accelerated-ion spectral shape, accelerated and ambient composition, and interacting-particle angular distribution. An example of such a spectrum is shown in Figure 2 for an isotropic accelerated-particle angular distribution. The nuclei responsible for the strongest lines are indicated.

### 2.3 Acceleration and interaction parameters

Table 1 summarizes the acceleration and physical parameters of our loop transport and interaction model that affect the measurable quantities addressed by our calculations. Deriving well-constrained values for those parameters is challenging. Previous analyses often ignored the complicated inter-dependences, relying on assumptions that resulted in unrealistically small uncertainties. Fortunately, the detailed dependences on the parameters can be quite different for each of the measurable quantities. Obtaining meaningful constraints on the parameters while addressing such dependences can be achieved for a given flare if the available measurements cover a sufficiently-broad range of the measurable quantities.

### 3. Observable Quantities Associated with Gamma-Ray Lines

The measurable quantities associated with a nuclear deexcitation line are the emission time history and the line fluence, shape and central energy. The aspects of an interacting accelerated ion that most significantly affect these quantities are (1) its direction of motion at interaction, (2) its kinetic energy at interaction, (3) the time of the interaction after release from the acceleration region, and (4) where in the loop it interacts. The parameters listed in Table 1 combine to affect all of these aspects and we discuss some of the dependences here: the interaction time history, the interacting angular distribution, the interaction depth distribution, and line ratios. For illustration, we use calculations of 4.44 MeV  $^{12}\text{C}$  nuclear deexcitation line production, but the results are qualitatively valid for other deexcitation lines. Except for the particular parameter being discussed and varied, the calculations that follow are performed for a power-law spectral index  $s = 4$ ,  $\delta = 0.20$ ,  $L = 11,500$  km,  $\lambda = 300$  and the atmosphere is that of Avrett (1981).

#### 3.1 Interaction time history

In the absence of magnetic convergence ( $\delta = 0$ ), ions do not mirror and the nuclear interaction time history depends only on the energy loss rate in the lower chromosphere and upper photosphere where the density is greatest and most of the interactions occur. In the presence of magnetic convergence ( $\delta \neq 0$ ), ions with initial pitch angles lying close to the loop axis also do not mirror (they are within the “loss cone”) and behave similarly. Ions outside the loss cone mirror and lose energy much more slowly as they traverse the low-density corona. These interactions thus occur on longer time scales, with the time scale increasing with increasing convergence. Figure 3 shows  $^{12}\text{C}$  line production time histories from accelerated particles released instantaneously at  $t = 0$  for  $\delta = 0.0, 0.20$ , and  $0.45$ . For the time histories with  $\delta \neq 0$ , the excesses at times less than 1 second are due to ions within the loss cone interacting on their first pass down the loop leg.

Pitch angle scattering causes the loss cone to be continuously repopulated. As a result, the nuclear interaction rate increases at early times and correspondingly decreases at later times. Decreasing  $\lambda$  below  $\sim 20$  no longer affects the time history because the rate of loss-cone replenishment then exceeds the rate of nuclear reactions in the loss cone. This is referred to as saturated PAS. Increasing the loop length increases the time scale of the interaction rate since mirroring particles spend more time at lower coronal densities where nuclear reactions are less likely.

The accelerated-ion spectral index has no significant effect on the interaction rate time history at times later than about 1 second after particle release. The larger fraction of interacting high-energy ions in harder spectra arrive at the footpoints on their first transport down the loop leg sooner, causing an increase in the rate before about 1 second. Similarly, different energy dependences of the interaction cross sections affect the time history only before  $\sim 1$  second.

Because the lifetimes of the excited states are very short, the measured line time history directly reveals the time history of the interaction rate. If the time history of the release of the particles from the acceleration site can be estimated, the measured flux can be used to constrain the physical parameters. For example, because electrons producing hard X-ray bremsstrahlung are relativistic, their transport time from the acceleration site to the interaction site is much less than that of ions. Assuming then that the measured hard X-ray flux represents the release time, the delay of the measured deexcitation line flux can constrain  $\lambda$  and  $\delta$ .

Predicted  $\gamma$ -ray line-emission time histories can be calculated from the time histories calculated above for instantaneous accelerated-particle release if the acceleration release time history is known. Figure 4 shows the  $<300\text{keV}$  electron bremsstrahlung measured by BATSE and the total narrow deexcitation line flux measured by

OSSE for the 1991 June 4 flare (Murphy et al. 1997). Using the X-ray flux as the release time history, predicted deexcitation line time histories are also plotted in Figure 4 for several values of  $\lambda$ . Assuming a loop length of  $2 \times 10^4$  km then provides 1- $\sigma$  upper limits of  $\lambda < 100$  and  $\delta < 0.2$ , implying that (1) there must be pitch-angle scattering present in flare loop where the accelerated particles propagate and (2) that magnetic convergence cannot be so high as to prevent the particles from quickly reaching the lower depths of the atmosphere where the interactions take place.

### 3.2 Interacting ion angular distribution

In the absence of magnetic convergence ( $\delta = 0$ ), there is no mirroring and the angular distribution of the interacting ions (assumed to be isotropic when initially released at the top of the loop) will be downward isotropic regardless of level of PAS or loop size. In the presence of magnetic convergence ( $\delta \neq 0$ ) but no PAS ( $\lambda \rightarrow \infty$ ), ions with pitch angles too small to mirror enter the “loss cone” and either undergo a nuclear reaction as they are moving downward or are thermalized. But most ions have larger initial pitch angles which results in mirroring and the interactions occur mostly at the ion mirror points where the density is greatest. Thus, most particles are moving parallel to the solar surface when they interact (i.e., a “fan beam” angular distribution) with a relatively small contribution from downward-moving ions. This downward contribution becomes even less important as  $\delta$  increases. Figure 5a shows the effect of magnetic convergence on the interacting ion angular distribution for  $\delta = 0.0, 0.20$  and  $0.45$ . For all of these calculations there is no PAS ( $\lambda \rightarrow \infty$ ). The distributions are plotted vs  $\mu = \cos(\theta)$  where  $\theta$  is the angle from the solar radius with  $\mu < 0$  pointing down into the Sun.

By continuously repopulating the loss cone, the effect of PAS is to produce more downward-directed interacting particles. This is seen in Figure 5b where angular distributions are shown for  $\lambda \rightarrow \infty$ ,  $\lambda = 300$ , and  $\lambda = 20$ . As PAS is increased ( $\lambda$  decreased), more particles interact in the loss cone and the distribution becomes more downward-directed until saturation is reached ( $\lambda \approx 20$ ).

The angular distribution of the accelerated ions when they interact is not significantly affected by the spectral index or by the energy dependence of the interaction cross section.

The angular distribution of the interacting particles influences the recoil direction of the excited nucleus which affects the observed  $\gamma$ -ray energy. Depending on the angle of observation, the observed energy is Doppler-shifted from the rest-frame energy. Figure 6 shows calculated line shapes (with  $\alpha/p = 0.5$ ) for a flare occurring at the center of the solar disk (heliocentric angle  $\theta_{\text{obs}} = 0$ ) for three interacting angular distributions: isotropic, downward beam and the distribution arising from saturated PAS transport ( $\lambda = 20$ , see Figure 5b). As the angular distribution becomes more downward directed, the amount of red-shift increases. The shift is less for flares occurring at larger  $\theta_{\text{obs}}$  so that at the solar limb the shift is negligible. Comparison of such calculated line shapes with data can then constrain the interacting angular distribution.

Figure 7 (from Smith et al. 2004) shows the combined percent red shift of the deexcitation lines measured (Share et al. 2002) by *SMM* for a number of flares occurring at various  $\theta_{\text{obs}}$  (averaged into six angle bins) and by *RHESSI* for the 2002 July 23, 2003, October 28 and 2003 November 3 flares. (Because the Doppler shift should be inversely proportional to the mass of the recoil nucleus, the red shifts of the individual lines have been multiplied by the nuclear masses for combining.) The *SMM* results clearly show a trend of red shift with  $\theta_{\text{obs}}$ , implying that the interacting angular distribution cannot be isotropic. Moreover, the surprisingly large red shift for the July 23 flare observed by *RHESSI* implied that not even a perfectly downward-beamed distribution was sufficient, prompting Smith et al. (2003) to suggest that the magnetic loop must be inclined from the vertical to the solar surface toward the Earth.

### 3.3 Interaction depth distribution

In the absence of magnetic convergence ( $\delta = 0$ ), there is no mirroring and the depth distribution reflects the grammage required for the accelerated particles to interact as they move downward through the solar atmosphere. In the presence of magnetic convergence ( $\delta \neq 0$ ), mirroring results in interactions occurring at higher elevations (and therefore lower densities) as more and more particles are prevented from penetrating the lower atmosphere. Even with minimal convergence, the lack of PAS ( $\lambda \rightarrow \infty$ ) results in a significant fraction of the interactions occurring at low densities; for no PAS, almost 20% of the interactions occur at densities less than  $10^{10}$

$\text{H cm}^{-3}$  for  $\delta = 0.2$  (this correspondingly increases the interaction time history, see 3.1 above). As PAS is increased ( $\lambda$  decreased), the bulk of the interactions move to higher densities as more interactions occur within the loss cone. The effect of loop length on the interaction depth distribution is minimal because transport through the low density corona has little effect on where the interaction will ultimately occur, assuming the other parameters are not changed.

Because higher-energy particles tend to interact farther along their paths, harder particle spectra result in interactions occurring at higher densities since more particles of higher energies are producing the interactions. This is seen in Figure 8a for  $s = 3, 4$  and  $5$ . The bulk of the interactions occur at chromospheric densities near  $10^{14} \text{ cm}^{-3}$ . Interactions whose cross sections have high thresholds tend to interact at higher densities, again the consequence of the longer ranges of higher-energy particles. This is seen in Figure 8b where the depth distributions for interactions with two different cross section energies are shown: a low threshold energy ( $\sim 1 \text{ MeV nucleon}^{-1}$ , similar to that of the  $1.634 \text{ MeV } ^{20}\text{Ne}$  deexcitation line) and a high threshold energy ( $\sim 25 \text{ MeV nucleon}^{-1}$ , similar to those of neutron-producing p- $\alpha$  reactions).

### 3.4 Line Ratios

Interactions of accelerated protons and  $\alpha$  particles with ambient heavy nuclei produce deexcitation lines that are only slightly broadened ( $\sim 2\%$  FWHM) due to the relatively-limited Doppler shift of the recoil excited nucleus. Interactions of accelerated heavier nuclei with ambient H and He produce broader lines ( $\sim 20\%$  FWHM) since the excited nucleus continues with relatively little loss of its initial energy. The acceleration parameters that affect the relative intensities of the narrow lines are the accelerated  $\alpha$ /proton ratio and the spectral index. Both accelerated protons and  $\alpha$  particles contribute to essentially all reactions producing excited nuclei via direct excitation or spallation and the relative contributions from the two particles vary according to the reaction cross sections. The fluence ratio of two lines whose production cross sections have markedly different energy dependences is sensitive to the steepness of the accelerated-ion spectrum. The  $6.129 \text{ MeV } ^{16}\text{O}$  and the  $1.634 \text{ MeV } ^{20}\text{Ne}$  lines are uniquely useful in this way because (1) the threshold for the  $^{20}\text{Ne}$  line is unusually low ( $\sim 2 \text{ MeV}$  for proton reactions and  $\sim 1 \text{ MeV nucleon}^{-1}$  for  $\alpha$  reactions) and is very different from that of the  $^{16}\text{O}$  line ( $\sim 7 \text{ MeV}$  for proton reactions and  $\sim 2.5 \text{ MeV nucleon}^{-1}$  for  $\alpha$  reactions), (2) they are both strong lines, and (3) they both arise from elements with high first ionization potential (FIP) and are therefore expected to be free of the abundance variations associated with low FIP elements (Murphy et al. 1991, Share & Murphy 1995, Ramaty et al. 1995, see below). Because both of these lines are prompt (the half-lives of the excited nuclei being  $< 10^{-10} \text{ s}$ ), the time dependence of this ratio provides an instantaneous measure of the spectral index.

Power-law spectral indexes have been determined from this ratio for a number of flares observed by several detectors over the past two solar cycles (e.g., Ramaty et al. 1996, Murphy et al. 1997, Ramaty & Mandzhavidze 2000, Emslie et al. 2004). The results of Ramaty et al. 1996 are shown in Figure 9 where an occurrence histogram of spectral indexes determined from this ratio measured for a number of *SMM* flares (Share & Murphy 1995) is shown. Most flare accelerated-particles have power-law spectral indexes from  $3.5$ – $5.5$ . This ratio was used by Ramaty & Mandzhavidze (2000) to establish the near energy-equivalency of accelerated ions and electrons.

Using the loop formalism of Hua et al. (1989), we also found that the escaping emission of these lines does not depend on the loop parameters because (1) the lines are not produced deep in the solar atmosphere and are therefore not attenuated, (2) the recoil velocities of the excited nuclei are non-relativistic so there is no significant beaming of the emission, and (3) our assumption of isotropic  $\gamma$ -ray emission in the excited nucleus rest frame. While the latter is not strictly true (see Dyer et al 1981), the results should not be significantly affected except for highly-beamed angular distributions which generally do not occur. Therefore, the only physical parameter affecting line ratios is the relative abundances of the ambient nuclei.

The ambient abundances where the accelerated particles interact were first determined by Murphy et al. (1991) using *SMM* data from the 1981 April 27 solar flare. The analysis showed that the abundances of Mg, Si and Fe relative to C and O are consistent with coronal abundances; that is, enhanced relative to photospheric abundances in accordance with their FIP. Using *SMM*  $\gamma$ -ray data from 19 flares, Share & Murphy (1995) showed that the ratios of line fluences from low FIP elements to those from high FIP elements vary from flare to flare by as much as a factor of 4, suggesting that the high FIP-to-low FIP element abundance ratios in the  $\gamma$ -ray

production region also vary by about this factor. On the other hand, the line fluence ratios from elements in the same FIP group showed either no statistically-significant variations or variations that could be interpreted as due to changes of the accelerated particle energy spectrum from flare to flare. Ramaty et al. (1996) used the *SMM* fluences to directly derive ambient abundances, confirming the coronal-like FIP dependence and flare-to-flare variability, as shown in Figure 10. Thus, it is now well established that the FIP effect is already present at the chromospheric densities where  $\gamma$ -ray lines are formed:  $10^{14}$ – $10^{15}$  cm<sup>-3</sup> (see Figure 8).

## Acknowledgements

We wish to acknowledge Xin-Min Hua, Reuven Ramaty and Benz Kozlovsky for their contributions to this research. Part of this research was supported by NASA DPR S92680F and W19977 and by ONR.

## References

- Aschwanden, M. J., Kosugi, T., Hudson, H. S., et al., The Scaling Law Between Electron Time-of-Flight Distances and Loop Lengths in Solar Flares, *ApJ* 470, 1198-1217, 1996.
- Aschwanden, M. J., Particle Acceleration and Kinematics in Solar Flares – A Synthesis of Recent Observations and Theoretical Concepts, *Sp. Sci. Rev.* 101, 1-227, 2002.
- Avrett, C. W., Models of the Solar Atmosphere, in: L. E. Cram & J. H. Thomas (eds.), *The Physics of Sunspots*, AURA, Sacramento Peak Observatory, p. 235-254, 1981.
- Dyer, P., Bodansky, D., Seamster, A. G., et al., Cross Sections Relevant to Gamma-Ray Astronomy: Proton-induced Reactions, *Phys. Rev. C* 23, 1865-1882, 1981.
- Emslie, A. G., Kucharek, I. H., Dennis, B. R., et al., Energy Partition in Two Solar Flare/CME Events, *JGR* 109, A10104-A10118, 2004.
- Hua, X.-M., R. Ramaty & Lingenfelter, R. E. Deexcitation Gamma-Ray Emission from Solar Flare Magnetic Loops, *ApJ* 341, 516-532, 1989.
- Kozlovsky, B., Murphy, R. J., & Ramaty, R., Nuclear Deexcitation Gamma-Ray Lines from Accelerated Particle Interactions, *ApJS* 141, 523-541, 2002.
- Masuda, S., Kosugi, T., Hara, H., et al., A Loop-top Hard X-ray Source in a Compact Solar Flare as Evidence for Magnetic Reconnection, *Nature*, 371, 495-497, 1994.
- Miller, J. A., Cargill, P. J., Emslie, A. G., et al., Critical Issues for Understanding Particle Acceleration in Impulsive Solar Flares, *JGR* 102, No. A7, 14631-14659, 1997.
- Murphy, R. J., Ramaty, R., Kozlovsky, B., & Reames, D. V., Solar Abundances from Gamma-Ray Spectroscopy: Comparisons with Energetic Particle, Photospheric and Coronal Abundances, *ApJ* 371, 793-803, 1991.
- Murphy, R. J., Share, G. H., Grove, J. E., et al., Accelerated Particle Composition and Energetics and Ambient Abundances from Gamma-Ray Spectroscopy of the 1991 June 4 Solar Flare, *ApJ* 490, 883-900, 1997.
- Ramaty, R., Kozlovsky, B. & Lingenfelter, R. E., Nuclear Gamma-rays from Energetic Particle Interactions, *ApJS* 40, 487-526, 1979.
- Ramaty, R., Mandzhavidze, N., Kozlovsky, B., & Murphy, R. J., Solar Atmospheric Abundances and Energy Content in Flare-Accelerated Ions from Gamma-Ray Spectroscopy, *ApJ* 455, L193-196 1995.
- Ramaty, R., Mandzhavidze, N., & Kozlovsky, B., Solar Atmospheric Abundances from Gamma-Ray Spectroscopy, in: R. Ramaty, N. Mandzhavidze, & X.-M. Hua (eds.), *High Energy Solar Physics*, Am. Inst. Phys., New York, 374, 172-183, 1996.
- Ramaty, R., & Manzhavidze, N., Gamma-rays from Solar Flares, in: P. C. H. Martens, S. Tsuruta, M. A. Weber (ed.), *IAU Symp.* 195, Am. Inst. Phys., San Francisco, p. 123-132, 2000.
- Reames, D. V., Magnetic Topology of Impulsive and Gradual Solar Energetic Particle Events, *ApJ* 571, L63-66 2002.
- Share, G. H., & Murphy, R. J., Gamma-Ray Measurements of Flare-to-Flare Variations in Ambient Solar Abundances, *ApJ* 452, 933-943, 1995.
- Share, G. H., Murphy, R. J., Kiener, J., & de Sereville, N., Directionality of Solar Flare Accelerated Protons and  $\alpha$ -particles from  $\gamma$ -ray Line Measurements, *ApJ* 573, 464-470, 2002.
- Smith, D. M., Share, G. H., Murphy, R. J., et al., High Resolution Spectroscopy of Gamma Ray Lines from the X-Class Solar Flare of 2002 July23, *ApJL* 595, L81-84, 2003.
- Smith, D. M., this volume, 2004.
- Sturrock, P. A., Weber, M., Wheatland, M. S., & Wolfson, R., Metastable Magnetic Configurations and Their Significance for Solar Eruptive Events. *ApJ* 548, 492-496 2001.
- Zweibel, E. G., & Haber, D., The Propagation of Energetic Ions in Magnetic Loops and Gamma Ray Emission from Solar Flares, *ApJ* 264, 648-659, 1983.

Table 1. Acceleration and Physical Parameters

Type	Parameter
acceleration	power law index ( $s$ ) accelerated-particle composition acceleration time profile
physical	level of PAS ( $\lambda$ ) magnetic convergence ( $\delta$ ) loop half-length ( $L_c$ ) ambient composition atmosphere density, temperature and ionization model

### Figure Captions

- Figure 1. Schematic showing particle acceleration, transport, and interaction products during solar flares. (Yohkoh image from Masuda et al. 1994.)
- Figure 2. Calculated  $\gamma$ -ray spectrum. The excited nuclei responsible for the strongest lines are indicated.
- Figure 3. Calculated time histories of  $^{12}\text{C}$  4.44 MeV line production for several values of the magnetic field convergence parameter  $\delta$ . Time = 0 corresponds to the instantaneous particle release time. Calculations performed for  $s = 4$ ,  $L = 11,500$  km, and  $\lambda = 300$ .
- Figure 4. Measured time histories of the summed narrow lines from the 1991 June 4 flare observed by *CGRO/OSSE*. Also shown is the *BATSE* measured time history of the  $<300$  keV emission due to electron bremsstrahlung. Calculated time histories for several levels of PAS are overplotted.
- Figure 5. Calculated angular distributions of the interacting accelerated particles. Panel (a) shows distributions for no PAS ( $\lambda \rightarrow \infty$ ) and several values of the magnetic field convergence parameter  $\delta$  (and  $s = 4$  &  $L = 11,500$  km). Panel (b) shows distributions for several values of PAS (and  $s = 4$ ,  $\delta = 0.20$ , &  $L = 11,500$  km).  $\mu = \cos(\theta)$  where  $\theta$  is the angle from the outward normal.
- Figure 6. Calculated  $^{12}\text{C}$  4.44 MeV line profiles for three interacting accelerated-particle angular distributions for a flare located at the center of the solar disk. The accelerated  $\alpha$ /proton ratio is 0.5.
- Figure 7. Variation of combined measured red shifts (per unit atomic mass) of the narrow  $\gamma$ -ray lines as a function of flare location on the solar disk. The open diamonds are for the 19 *SMM* flares (averaged into 6 angle bins). The filled diamonds are for the 3 *RHESSI* flares on (1) 2001 July 23, (2) 2003 October 28, and (3) 2003 November 3.
- Figure 8. Fraction of nuclear reactions occurring at density greater than a given density in the solar atmosphere of Avrett (1989). Panel (a) shows the  $^{12}\text{C}$  excitation fraction for several values of the accelerated-particle spectra index  $s$  (and  $\delta = 0.20$ ,  $L = 11,500$  km, &  $\lambda = 300$ ). Panel (b) shows the fraction for two reactions, one with a low threshold energy ( $\sim 1$  MeV) and one with a high threshold energy ( $\sim 25$  MeV) and  $s = 4$ ,  $\delta = 0.02$ ,  $L = 11,500$  km &  $\lambda = 300$ .
- Figure 9. Distribution of power law spectral indexes derived from the ratio of the 6.31 MeV  $^{16}\text{O}$  and 1.63 MeV  $^{20}\text{Ne}$  flux ratio.
- Figure 10. Derived ambient Mg/O, Mg/Ne, Si/O and Fe/O abundance ratios. The solid lines are the coronal (Cor) and photospheric (Pho) values. The dashed lines are averages of the measured values. For Si/O and Fe/O, not all flares could be measured.

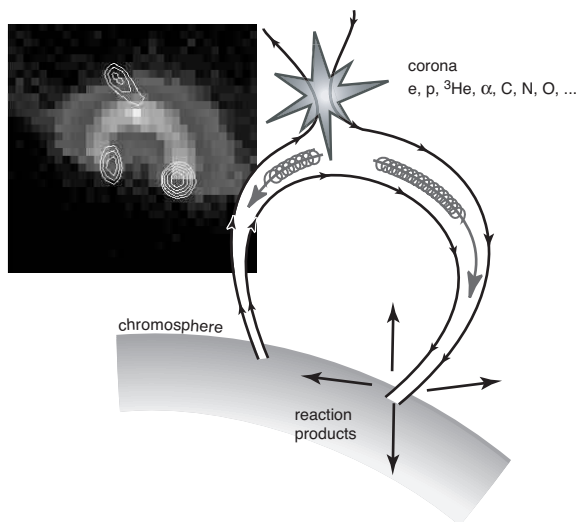


Fig 1

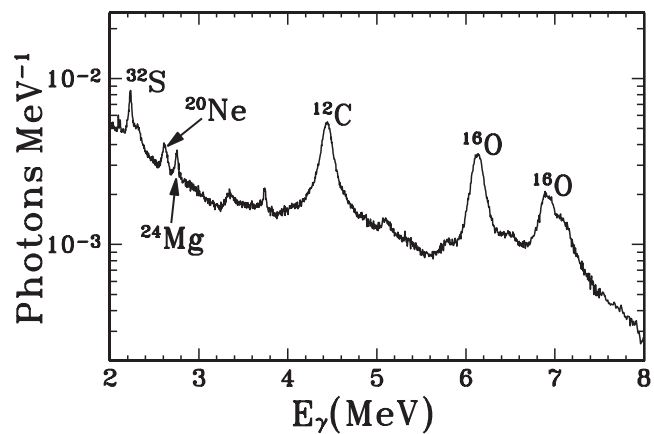
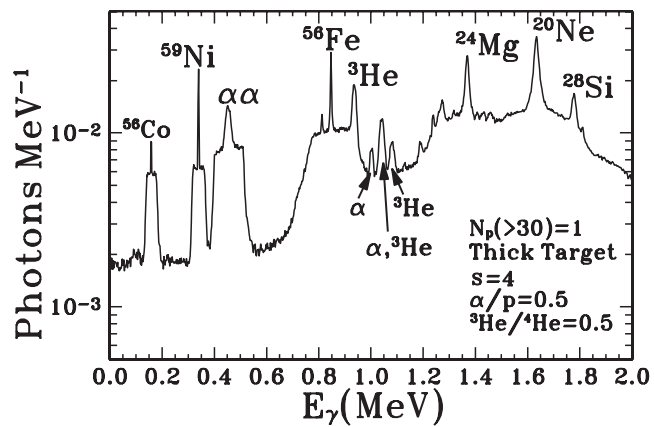


Fig 2

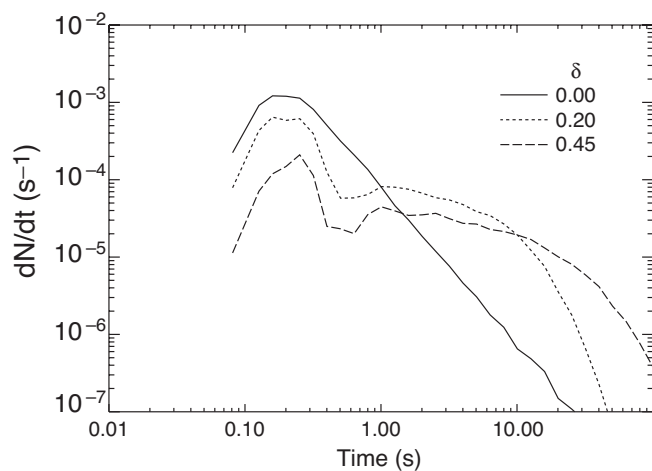


Fig 3

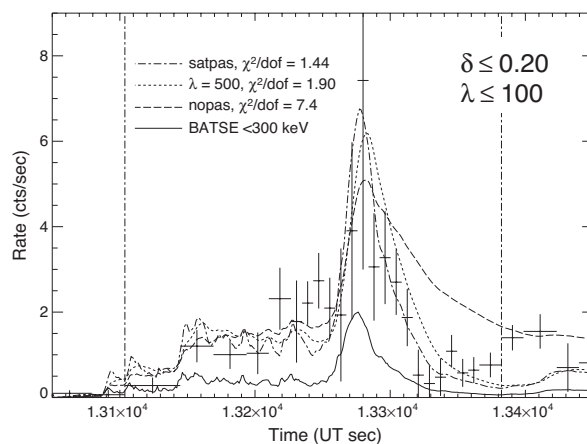


Fig 4



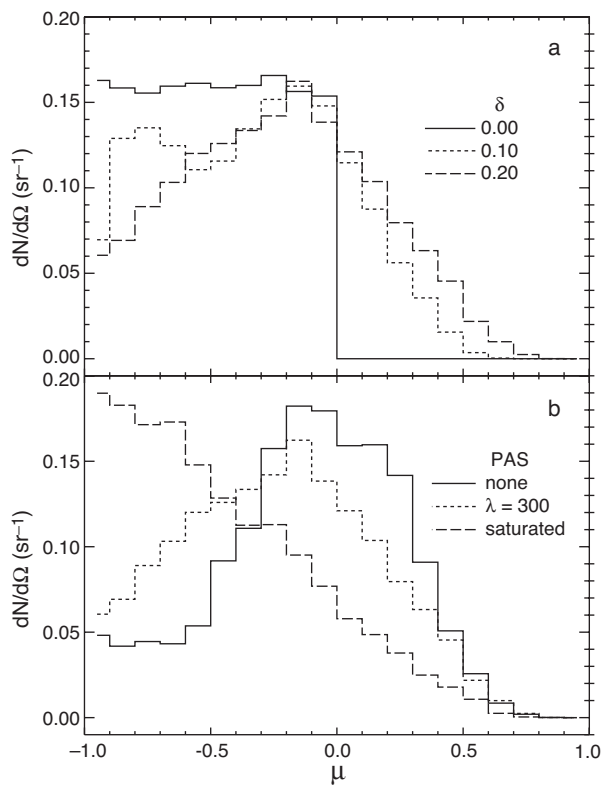


Fig 5

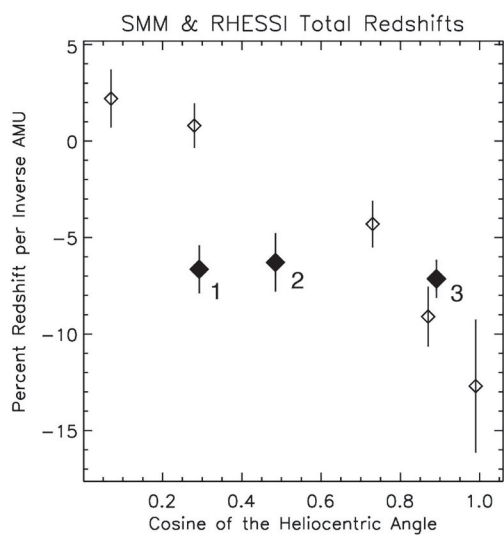


Fig 7

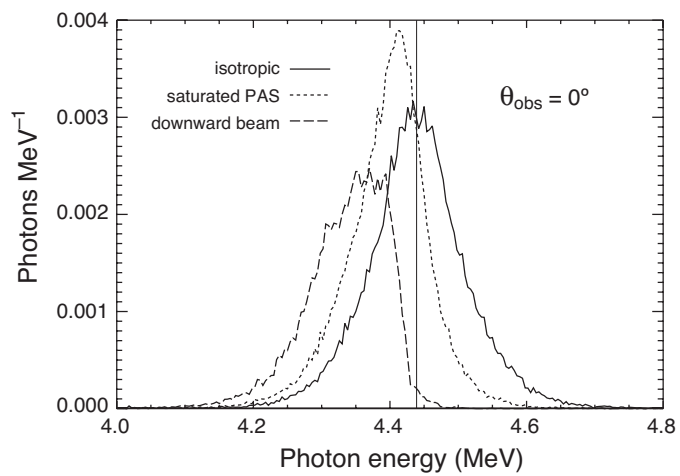


Fig 6

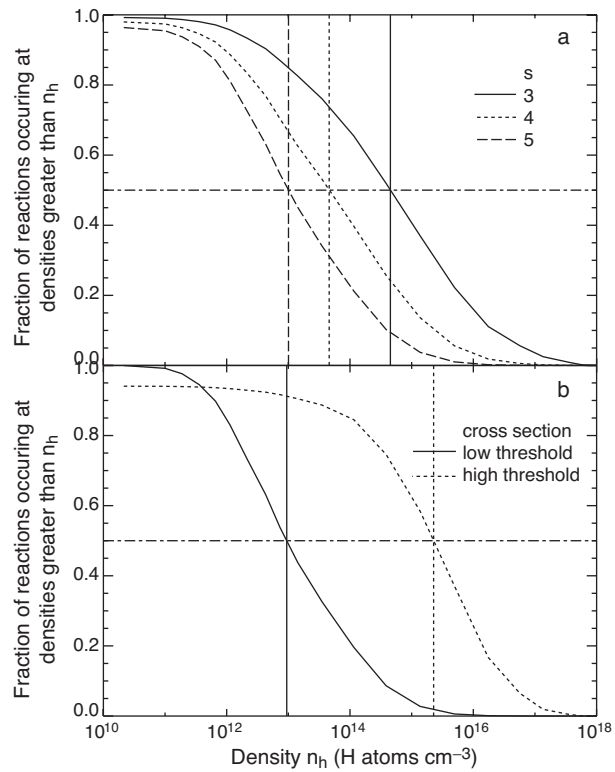


Fig 8

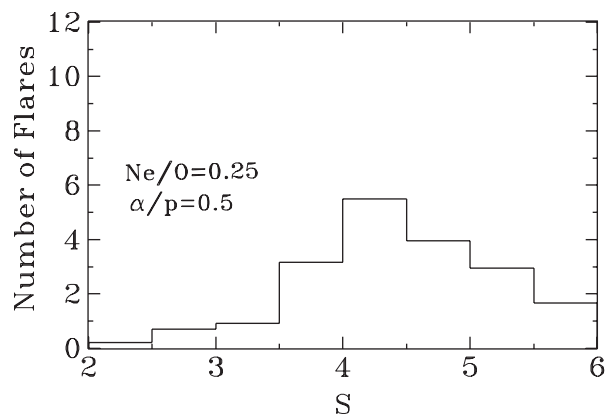


Fig 9

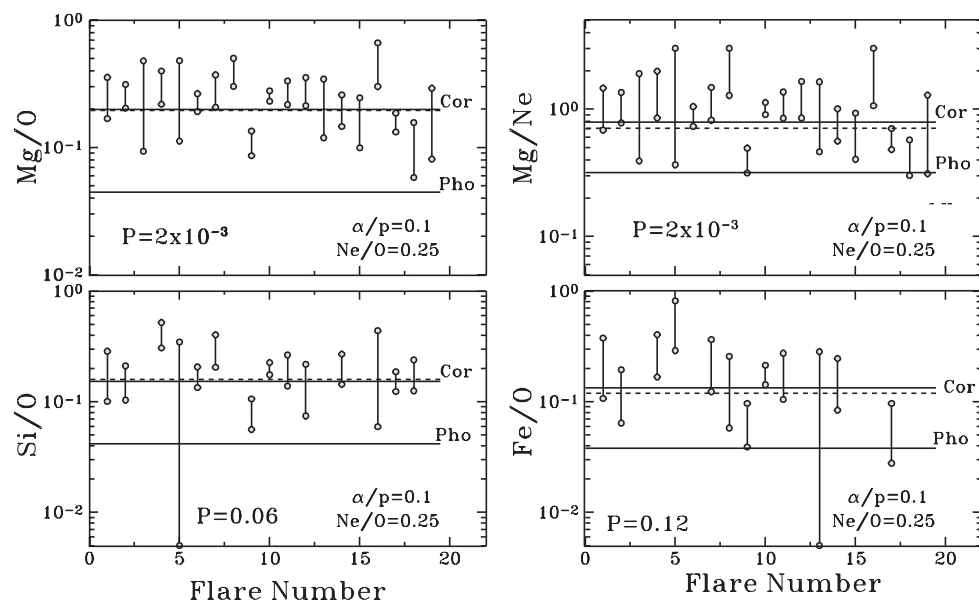


Fig 10